Low-Frequency Oscillations in Hypersonic Cavity Flows with Increased Rear-Wall Height

S. Sharma*, P. Moise* and S. R. Nanda*
Corresponding authors: pmoise@iitk.ac.in, srnanda@iitk.ac.in
* Indian Institute of Technology Kanpur, India.

Abstract: Open cavity flows occur in a variety of situations, including weapon bays and landing gear wells. Their dynamics are typically characterized by Rossiter modes, with modes of different frequencies dominating at different geometric and flow parameters. While cavities of equal front- and rear-wall heights have been the focus of intense research, asymmetric cavities with increased rear-wall height have received little attention, especially in the hypersonic regime, owing to their tendency to enhance flow oscillations. However, such configurations may find relevance in thermal protection systems, future scramjet combustor designs, weapons, and payload compartments. Motivated by this, the present study examines the effect of rear-wall height on flow features and unsteadiness in open cavity flows. To study the same under hypersonic conditions, the two-dimensional compressible Navier–Stokes equations are numerically solved for a freestream Mach number of $M_\infty = 6$ with rear-wall-to-front-wall height ratios, h_r/h of 0.5, 1.0, 1.5, and 2.0. This parameter was observed to significantly affect which Rossiter mode dominates the flow, indicating the strong influence of the rear wall in determining the flow dynamics. Further, increased rear-wall heights were observed to influence regions upstream of the cavity leading edge, causing the separation point to migrate upstream of the cavity leading edge. The highest rear-wall configuration studied ($h_r/h = 2.0$) was found to exhibit a low-frequency oscillation (LFO), in which the separation location oscillates in the streamwise direction at a frequency significantly lower than the Rossiter modes, indicating a new flow instability in cavity flows. Spectral proper orthogonal decomposition revealed that this LFO is characterized by a large-scale global periodic motion that is visually similar to that of transonic buffet in airfoil flows. These results highlight several new features of open cavity flow dynamics in the hypersonic regime, which can be potentially harnessed for novel hypersonic combustor and vehicle designs.

Keywords: Hypersonic flow simulations, Cavity flows, Low-frequency oscillations

1. Introduction

When a high-speed boundary layer encounters a rectangular cavity, the flow separates at the leading edge and can form a shear layer spanning the entire cavity and reattaching near the trailing edge – i.e., an open cavity flow [1]. Open cavity flows have been studied extensively as they occur in various aerospace applications, such as internal weapon bays in military aircraft, landing gear wells, launch vehicles, scramjet combustors, thermal protection system gaps, etc. Typical open cavity flows are inherently unstable and develop self-sustained oscillations in which vortical structures shed from the upstream cavity edge, convect downstream, and impinge on the trailing edge. This impingement generates upstream-traveling acoustic waves that trigger the formation of new vortices at the leading edge. This feedback process results in discrete resonant frequencies, referred to as Rossiter modes [2]. Since the unsteadiness caused by Rossiter modes is detrimental to vehicle performance, a major focus of open-cavity research has been on mitigating them. Research on these flow oscillations has shown that they are strongly influenced by geometric parameters such as cavity length, depth, and wall heights, rear-wall angle, as well as flow parameters such as freestream Mach number and Reynolds number. Although studies have examined cavities with unequal front- and rear-wall heights (h and h_r, respectively), the focus has been on lower rear-wall height ($h_r/h < 1$), as it reduces flow unsteadiness [3] and geometries with $h_r/h > 1$ remain relatively less explored, especially in the hypersonic regime. However, understanding the influence of higher rear-wall height can shed further light on the dynamics of open-cavity flows. Motivated by this, the present computational study examines the effect of varying the rear-wall to front-wall height ratio h_r/h on hypersonic open-cavity flows, with a focus on positive-offset ($h_r/h > 1$).

Since the early studies of Karamcheti [4] and Rossiter [2], cavity-flow research has evolved considerably across subsonic, transonic, supersonic, and hypersonic regimes [5, 1, 6, 7], and its major advancements have been compiled at various stages in the literature [8, 9]. Since its discovery, the Rossiter mechanism has been extensively investigated through experiments and CFD. Experimental investigations have deployed schlieren visualisations, wall-pressure measurements, and particle image velocimetry (PIV) to determine how Kelvin–Helmholtz instabilities develop and convect after leading-edge separation, which then interact with the trailing edge and produce upstream-traveling disturbances that close the feedback loop [1, 10]. Numerical simulations have provided more insight into the feedback mechanism in compressible flows [11]. Recent works have used modal decomposition techniques such as proper orthogonal decomposition (POD) and spectral POD (SPOD) to identify the coherent structures associated with Rossiter modes and their evolution in time and space [12, 13].

Abundant work has been conducted on cavity flows in the subsonic and supersonic regimes, but owing to the additional complexity and computational resources required, relatively limited literature exists for hypersonic cavity flows. A study by Wang *et al.* [14] in the supersonic regime revealed that, as the Mach number increases, the shear layer becomes stabilized and the strength of the oscillations decreases. Murray & Elliott [15] also reported that increasing the freestream Mach number reduces the size and coherence of the large-scale structures within the shear layer. Three-dimensionality of the flow is increased, and the shear layer is stabilised due to compressibility effects. Thus, it is reasonable to expect that the progressive stabilisation of the shear layer would be even stronger at hypersonic speeds, causing the oscillation amplitudes to be comparatively reduced. Morgenstern & Chokani [16] were among the first to discuss the self-sustained oscillation mechanism in hypersonic cavity flows at a freestream Mach number of $M_\infty = 6.3$ and investigate it computationally. Unalmis *et al.* [17] experimentally studied cavity flows at $M_\infty = 5$ and reported weak shear-layer/acoustic coupling. Bai *et al.* [18] studied equilibrium hypersonic cavity flows with a focus on cavity-induced transition resulting from the separation induced at the cavity's leading edge that generates strong shear-layer instabilities and the small-scale vortical structures present in the flow downstream of the cavity.

Besides the freestream Mach number, the freestream Reynolds number is another important parameter to consider while studying cavity flows. Previous studies have shown that the Reynolds number does not strongly affect the oscillatory behaviour of cavity flows [19, 20], but it can alter the properties of the incoming boundary layer, such as its thickness and state, and may cause it to transition from a laminar to a turbulent state. Karamcheti [4] observed that thin laminar boundary layers promote stronger oscillations and pressure fluctuations, whereas turbulent boundary layers, being inherently thicker and containing increased random fluctuations, weaken the feedback process and reduce the prominence of discrete tones. Similar results were reported by Scheiman [21], and Seena & Sung [22], who observed that a thick boundary layer did not exhibit significant oscillating pressures, whereas a thin boundary layer produced large-scale structures and formed a fully coherent dominant spectral peak. Hence, thin approaching boundary layers are associated with strong Rossiter-mode oscillations, whereas thicker boundary layers produce a more broadband response. Sun *et al.*[23] noted that three-dimensional effects reduce the amplitude of cavity oscillations by redistributing energy into spanwise modes, but the dominant frequencies remain largely unchanged.

Self-sustained oscillations can result in high noise and structural loading [24, 25]. Consequently, considerable effort has been devoted to suppressing these oscillations while retaining the favourable pressure gradients characteristic of open cavity flows. This can be achieved through various flow-control techniques. Among these, the passive approach of modifying the rear-wall inclination has received significant attention because it deintensifies the shear layer impingement on the aft wall compared to a conventional straight-wall rectangular cavity, thereby reducing the pressure fluctuations [26]. Vikramaditya [27] observed that, for inclination angles of 60° and below, no upstream-propagating acoustic waves were identified, resulting in the absence of a feedback loop. Other passive control techniques based on geometric modifications include sub-cavities inserted on cavity surfaces and leading-edge spoilers [28, 29, 30]. The present study, although not aimed at flow control, focuses on a rear-wall modification involving variations in rear-wall height and its effect on the oscillatory characteristics of the cavity flow.

Nanda *et al.* [31] explored the effect of rear-wall height variation in axisymmetric cavities at a freestream Mach number of $M_\infty = 6$ through experiments. They observed that increasing the rear-wall height causes a transition from a Kelvin–Helmholtz-dominated cavity flow with higher-order Rossiter modes to a pressure-driven flapping mode resembling a breathing mechanism, with the dominant frequency corresponding to the first Rossiter mode. These flow oscillations occur at a relatively lower frequency and dominate the cavity dynamics with larger amplitudes for sufficiently large rear-wall heights.

To the best of the authors' knowledge, no other studies have examined the effect of increased rear-wall height on the unsteady characteristics of high-speed cavity flows. To address this gap and analyse the effect of the geometric parameter, h_r/h, the two-dimensional planar compressible Navier-Stokes equations are numerically solved, and the results are analysed to examine flow features, including using a spectral proper orthogonal decomposition (SPOD). The rest of the article is organized as follows. The methodology, including the geometry and flow setup, governing equations, and numerical flow solver details, and SPOD are outlined in §2. Subsequently, the simulation results, including mean flow structure, dynamical features, and SPOD results, are discussed in §3. The conclusion is presented in §4.

2. Methodology

2.1 Flow setup

Features of the domain used in the study are shown in Figure 1. The two-dimensional, planar cavity studied is characterized by the cavity length L, front-wall height h, and rear-wall height, h_r. An aspect ratio of $L/D = 6$ is maintained for all configurations, while the rear-wall-to-front-wall height ratio, h_r/h, is varied from 0.5 to 2.0 in increments of 0.5. The front-wall height is chosen as the length scale and kept constant, and only the rear-wall height is varied to change the height ratio. The cavity configurations are named based on their rear-wall heights and are referred to as Case $0.5h$, $1.0h$, $1.5h$, and $2.0h$. A Cartesian coordinate framework is used, with x representing the streamwise direction and y, the wall-normal direction (assuming a planar, two-dimensional flow), with the origin located at the leading edge of the cavity.

The hypersonic flow is assumed not to involve any molecular dissociation, and the relevant governing equations are given by the compressible Navier-Stokes equations. The freestream Mach number is chosen as $M_\infty = 6$, while the freestream Reynolds number based on the front-wall height of the cavity is given by $Re_h = 2.0 \times 10^5$. The fluid is assumed to be an ideal gas with constant specific heats, which is considered appropriate for low-enthalpy flows. The specific heat ratio is $\gamma = 1.4$. The inflow boundary is assumed to be a uniform flow. At the inflow and top boundaries of the domain, freestream conditions are prescribed, and a zero-order extrapolation boundary condition is applied at the outlet. The upstream boundary to the cavity is split into free-slip and wall regions of length $5h$ each, in order to avoid the influence of inflow on the developing boundary layer. The cavity walls, cavity floor, and the downstream flat plate are wall regions. All walls are treated as no-slip isothermal surfaces. The flow is initialized with uniform freestream initial conditions at a lower Mach number of $M_\infty = 2$. Once the flow state is converged, the Mach number is ramped up in increments of 0.5, until the desired freestream conditions of $M_\infty = 6$ are reached.

2.2 Flow solver and numerical setup

The two-dimensional, unsteady compressible Navier–Stokes equations are solved in conservative form using the high-order, finite-difference, open-source flow solver, OpenSBLI (v3.0) [32]. It has been

Table 1: Flow and geometric parameters used in the present study.

M_∞	Re_h	Pr	γ	T_{wall}/T_∞	δ_0/h	h_r/h
6.0	2.0×10^5	0.71	1.4	5.0	0.0723	0.5, 1.0, 1.5, 2.0

applied to a wide range of compressible flow problems and has been extensively validated for multi-block implementation as well [32, 33, 34, 35, 36, 37, 38]. The Navier-Stokes equations are solved in a dimensionless form based on the front-wall height and freestream conditions. Convective fluxes are discretised using a fifth-order Weighted Essentially Non-Oscillatory (WENO5) shock-capturing scheme with Harten–Lax–van Leer–Contact with low-Mach-number correction (HLLC-LM) upwind flux splitting. Viscous fluxes are discretised using a fourth-order central finite-difference scheme. A third-order explicit Runge–Kutta scheme (RK3) is used for temporal marching. The time step used for all simulations is $\Delta t = 1 \times 10^{-5}$.

The two-dimensional computational domain comprises four or six structured blocks, depending on the cavity configuration. A representative layout of the multi-block domain for Case 2.0h with boundary conditions indicated is shown in Figure 1. The multi-block grid is generated using the commercial mesh-generating software, Pointwise™. The grid is Cartesian, and all individual blocks are structured. Clustering is applied for the grid points in both the streamwise and wall-normal directions. The minimum wall-normal spacing is maintained as $\Delta y_{\min} = 0.0001$ in all blocks. Although the flow is laminar, this spacing was chosen anticipating future extensions to three-dimensional simulations, by ensuring, *a posteriori*, that the wall-normal spacing in wall-units is $\Delta y^+ < 1$ at all walls. A sponge layer of thickness h is applied at the outlet and top boundaries to prevent reflections. The simulations are executed using the CUDA-MPI backend on multi-GPU clusters.

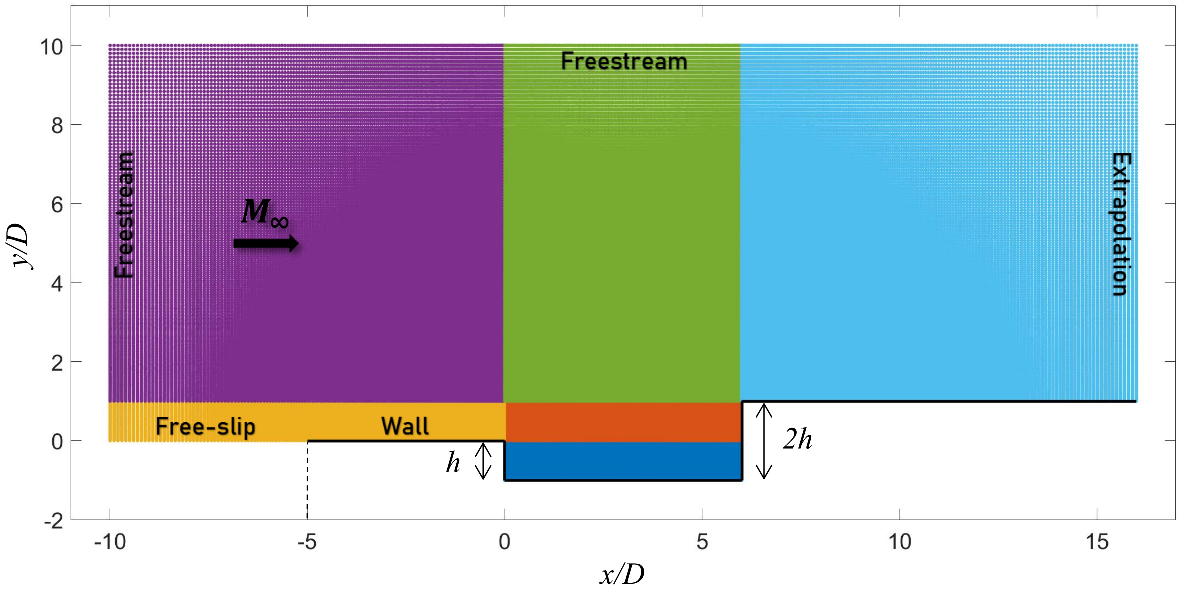

Figure 1: Multiblock computational domain for configuration 2.0h.

2.3 Grid Convergence

A grid convergence study is performed using three grids referred to as coarse, medium, and fine, containing approximately 5.62×10^5, 1.03×10^6, and 1.80×10^6 grid points, respectively. The configuration 2.0h is used as the benchmark to ensure that the simulation results are independent of the grid resolution. The total refinement ratio between successive grids is maintained at approximately 1.8, which corresponds to an increase of about 1.38 times in the number of grid points in each direction. The total number of points is effectively doubled in the cavity region. Grid convergence is assessed by comparing the time-averaged pressure and skin-friction coefficients, C_p and C_f on the cavity floor, and the power spectral density (PSD) of the pressure fluctuations at a specific location within the flow.

Figure 2(a–b) presents the variation of C_p and C_f along the cavity floor, respectively. There is excellent agreement between the results for the medium and fine grids, indicating that the former is adequate for capturing all mean flow features. Figure 3 shows the PSD spectra of pressure fluctuations obtained at the location $x/D = 3.0$, $y/D = -1.0$, which corresponds to the center of the cavity floor, for the three grids. The dominant frequency peaks coincide for the medium and fine grids at Strouhal number $St_h \approx 0.014$, thereby demonstrating excellent agreement. Differences in the secondary peaks are present due to modified numerical dissipation at smaller scales caused by the varying resolution, but since the dominant peaks and the primary flow characteristics remain the same, it is assumed that the medium grid is sufficiently resolved for capturing the dominant dynamics adequately. Thus, the medium grid or its equivalent is used for all subsequent simulations. Grid convergence is performed only for the $2.0h$ configuration, but care is taken that all other configurations follow similar meshing topology and clustering to ensure grid independence.

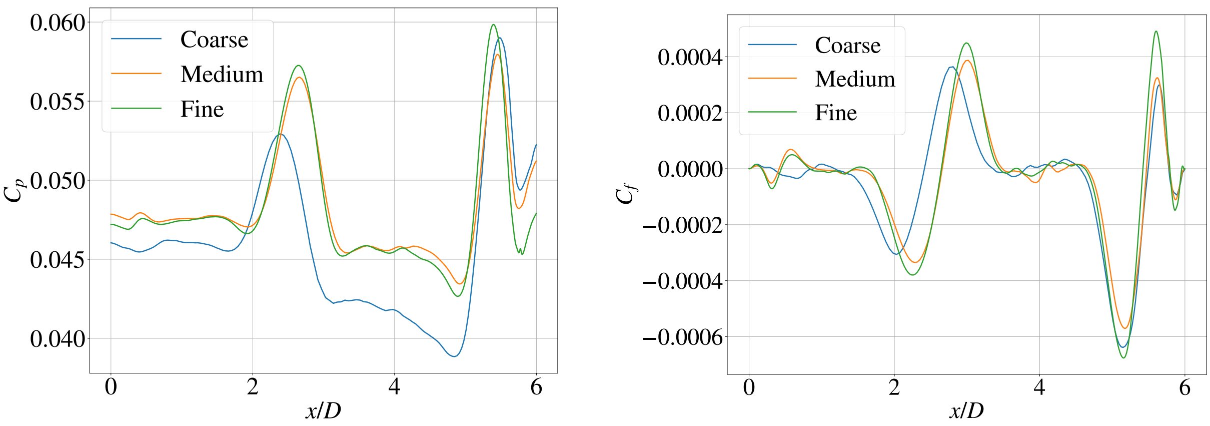

(a) C_p distribution (b) C_f distribution

Figure 2: Variation of (a) mean pressure coefficient C_p and (b) mean skin-friction coefficient C_f along the cavity floor for coarse, medium and fine grids.

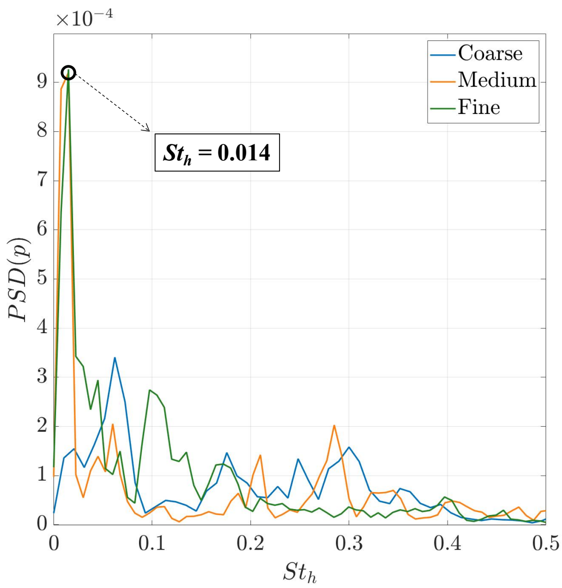

Figure 3: Power spectral density (PSD) of pressure fluctuations at the centre of the cavity floor ($x/D = 3.0$, $y/D = -1.0$) for the coarse, medium, and fine grids.

2.4 Verification Study

Prior to performing the parametric study on different rear-wall height configurations, a reference supersonic cavity flow case 'M4' from Ref. [39] is selected for verification. The reference study performed a two-dimensional Direct Numerical Simulation of an open-cavity flow at a freestream Mach number of $M_\infty = 2.1$ and a Reynolds number based on cavity depth of $Re_D = 4500$, with a prescribed incoming boundary-layer momentum thickness of $L/\theta_0 \approx 113.67$ or $\theta_0/D \approx 0.0352$, at the cavity leading edge. The cavity geometry is symmetric and has a length-to-depth ratio of $L/D = 4$. The self-sustained oscillations for this particular case are reported to correspond to Rossiter mode III. This study is chosen as the two-dimensional configuration is similar to the present simulations and provides detailed information on the flow organization, vortex shedding process, and dominant Rossiter frequencies, along with their comparison to semi-empirical relations, making it suitable for numerical verification. To replicate the aforementioned conditions, a precursor flat plate boundary-layer simulation is performed to determine the approximate upstream wall length required to achieve the target momentum thickness of $\theta_0/D \approx 0.0352$. The required upstream length was found to be approximately $2.7D$, which was used for the present simulation. Other aspects of the numerical setup used for the current simulation are similar to those used for the rest of the simulations in this study.

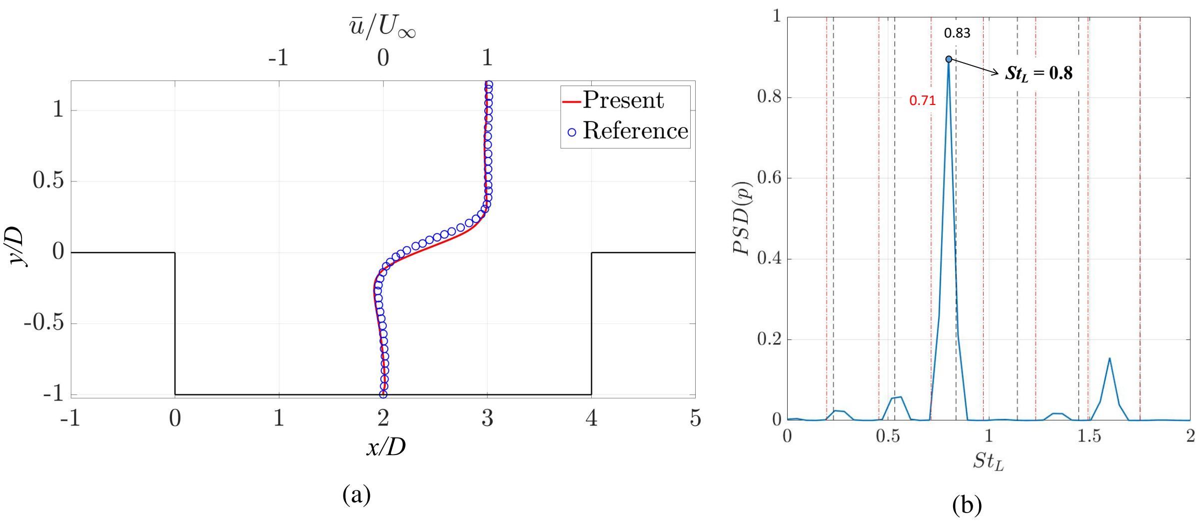

Figure 4: (a) Comparison of time-averaged streamwise velocity profile along the cavity centerline between the present simulation and the reference study (Ref. [39]), and (b) PSD of the pressure fluctuation data measured at location ($x/D = 3.9,\ y/D = 0.0$). Red dash-dot lines denote the frequency predictions from the original Rossiter relation [2], and black dashed lines denote the predictions from the modified Rossiter relation [1].

The time-averaged streamwise velocity profile extracted along the cavity centreline from the present simulation is compared with the reference data, as shown in Figure 4(a). Good agreement is observed between the two datasets in the cavity interior, shear layer, and freestream regions. Next, the frequency response of the cavities is compared. Figure 4(b) shows the power spectral density (PSD) of the pressure fluctuation data at a location within the shear layer ($x/D = 3.9,\ y/D = 0.0$). The dominant peak is observed at $St_L \approx 0.80$, which is within the analytical predictions from the original Rossiter relation [2] and modified Rossiter relation [1] of $St_L \approx 0.713$ and $St_L \approx 0.837$, respectively. Zhang *et al.* [39] reported a dominant frequency of $St_L \approx 0.698$, which also corresponds to Rossiter mode III but shows closer agreement with the original formula, while the present simulation result matches better with the modified relation. The slight discrepancy in the exact frequency location of Rossiter mode III could be due to numerical accuracy, as the reference study has used a second-order scheme while the present simulations utilize a fifth-order spatial discretisation scheme, resulting in lower numerical dissipation and improved accuracy. It is important to note that strong compressibility effects are present at $M_\infty = 2.1$.

The modified formula accounts for the compressibility effects that modify the speed of sound within the cavity, whereas the original relation assumes it to be the same as that in the freestream. Thus, the modified version is more physically representative for high-speed cavity flows. However, both studies correspond to the same dominant shear-layer mode (Rossiter mode III), and, together with the excellent agreement in the mean velocity profile, it is confirmed that the present solver and computational setup are capable of capturing the essential physics of high-speed cavity flows. Therefore, similar solver settings and setup are used in subsequent simulations for studying the effect of rear wall height variation on cavity flows.

3. Results and Discussion

3.1 Flow structure

The time-averaged local Mach number contours overlaid with mean streamlines in the cavity region are shown in Figure 5. The characteristic angles for all relevant features are also marked. Numerical Schlieren plots highlighting all the canonical features of instantaneous flow are shown in Figure 6. Note that for both figures, only part of the computational domain that is of interest is shown. A very weak shock wave is formed on the upstream flat plate as the freestream initially encounters the no-slip wall at $-5h$. It is referred to as "upstream-weak-shock wave" in the present study. The boundary layer separates and forms a free shear layer for all cases. The separation develops at the cavity lip for Cases $0.5h$ and $1.0h$, but occurs further upstream for Cases $1.5h$ and $2.0h$. Increasing the rear-wall height increases the separated shear-layer's inclination and shifts its trajectory upward, with Case $2.0h$ exhibiting the largest inclination. The size and confinement of the recirculation region, and hence the effective cavity volume is increased. For the negative-offset configuration ($h_r/h < 1$), Case $0.5h$, a downward shear-layer inclination is observed, leading to an expansion fan at the cavity's leading edge. The freestream interacts with the separated shear layer to form a separation shock wave for positive offset configurations ($h_r/h > 1$). For these positive offset conditions, it was observed that the separation location oscillates at a lower frequency than that of Rossiter modes, as detailed in subsequent discussions on the flow dynamics. We will refer to this phenomenon as a low-frequency oscillation (LFO). Thus, the mean separation shock wave associated with Case $2.0h$ appears smeared in the time-averaged flow because its instantaneous position varies with time due to LFO. The trailing-edge impingement shock wave is present in all cases. The free shear layer formed after separation spans the extent of the entire cavity across all cases. Thus, it is confirmed that all cases correspond to open-cavity flow.

Figure 7 shows the distributions of the mean pressure coefficient, C_p, and mean skin-friction coefficient, C_f, along the wall upstream to the cavity. Note that $x/D = 0$ represents the cavity leading-edge. Cases $0.5h$ and $1.0h$ bear nearly identical distributions indicating negligible upstream influence of the cavity's rear-wall height. Higher height-ratio Cases $1.5h$ and $2.0h$ show a clearly recognizable rise in C_p at approximately $4.6h$ and $2h$ upstream of the cavity leading edge, respectively, associated with the influence of an oscillating separation shock wave. The higher C_p values for Case $2.0h$ clearly show that the shock wave associated with it is the stronger. The C_f distributions complement the C_p results and highlight the mean separation locations, which lie at approximately $-4.25h$, just downstream of the separation shock for Case $2.0h$, and at approximately $-1.75h$ for Case $1.5h$. For Cases $0.5h$ and $1.0h$, the boundary layer stays attached throughout the upstream length, confirming that the separation occurs at the leading edge of the cavity.

3.2 Flow dynamics

The oscillatory flow dynamics of the cavity flows are discussed in this section by examining the evolution of flow field variables at specific locations in the domain and using Spectral Proper Orthogonal Decomposition (SPOD). Case $0.5h$ does not show any distinct oscillatory behavior and is not analyzed further. For the other cases, the temporal evolution of the pressure at a location just below the shear layer on the cavity centerline is compared in Figure 8. For the two positive offset cases studied, the flow dynamics showed an abrupt transition between two sufficiently long phases (based on flow through time) associated

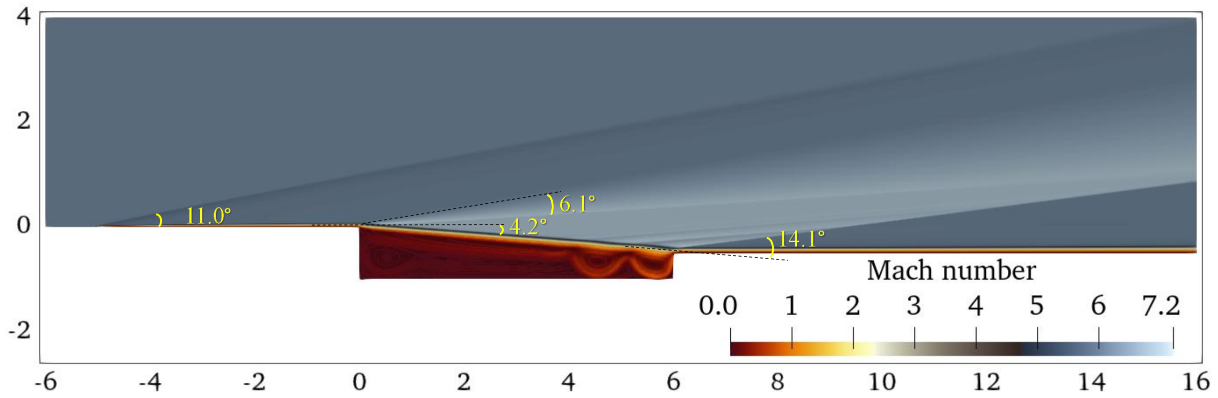

(a) Case 0.5h

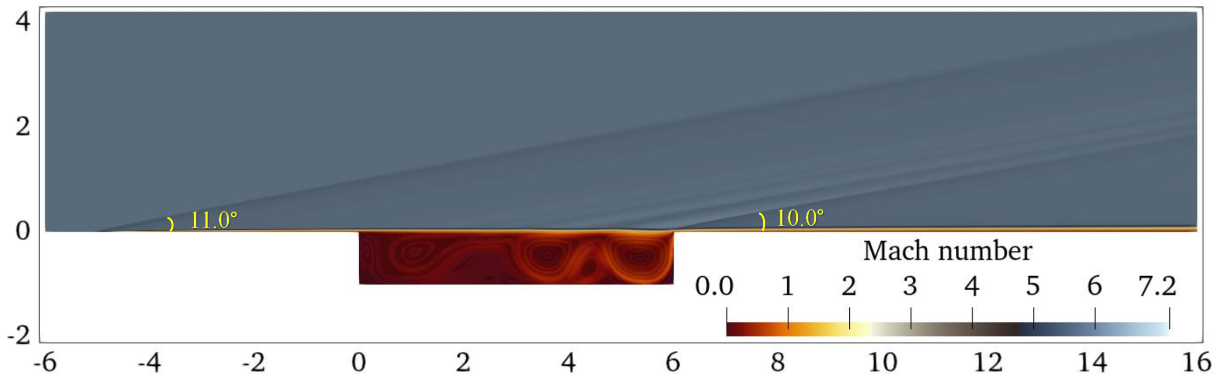

(b) Case 1.0h

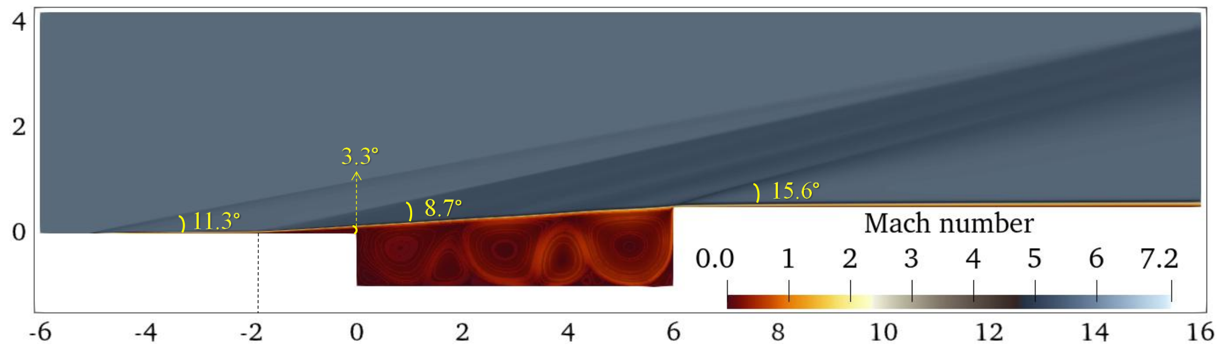

(c) Case 1.5h

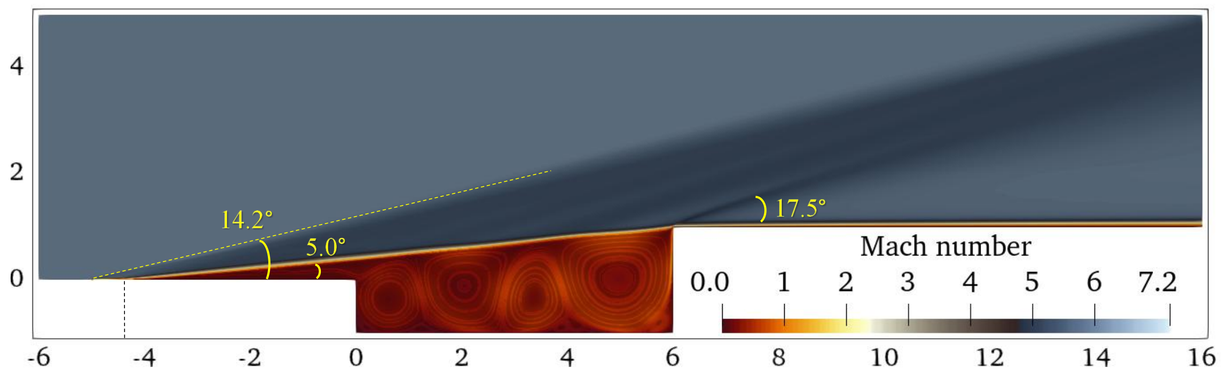

(d) Case 2.0h

Figure 5: Mean flow Mach number contours for all configurations with shear layer inclination angles and shock/expansion angles indicated.

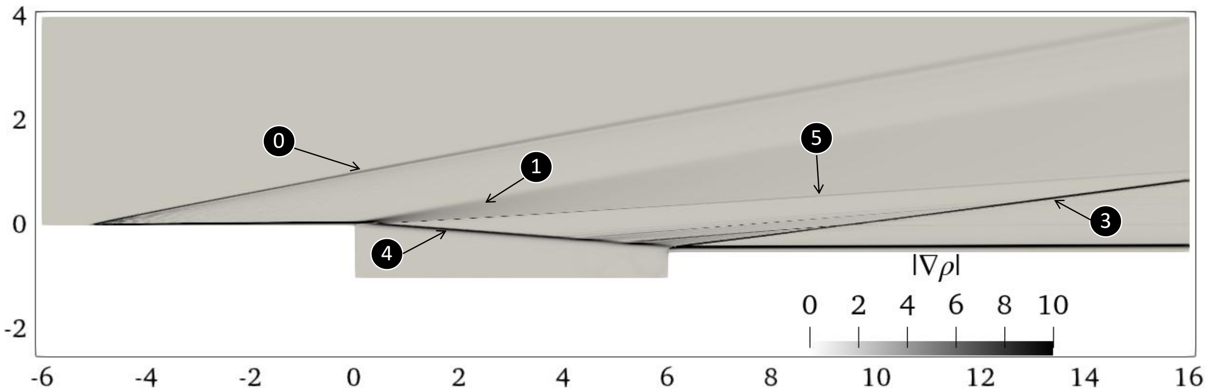

(a) Case 0.5h

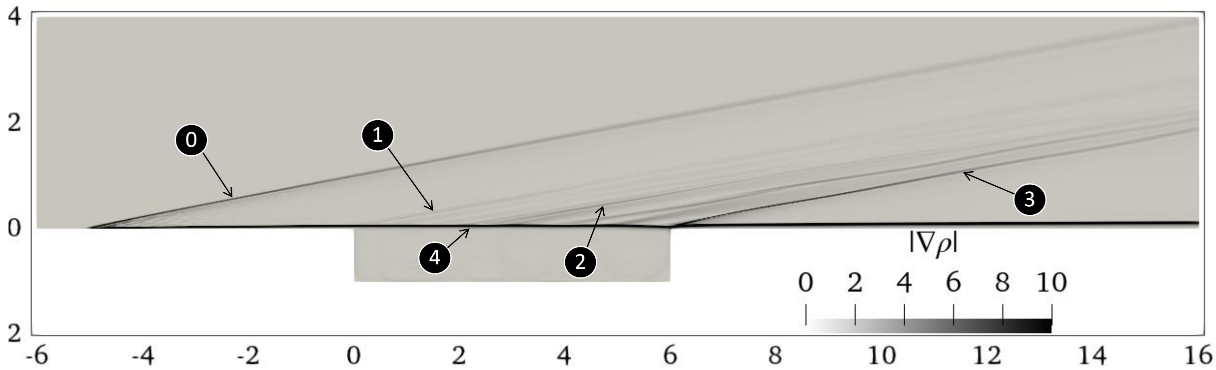

(b) Case 1.0h

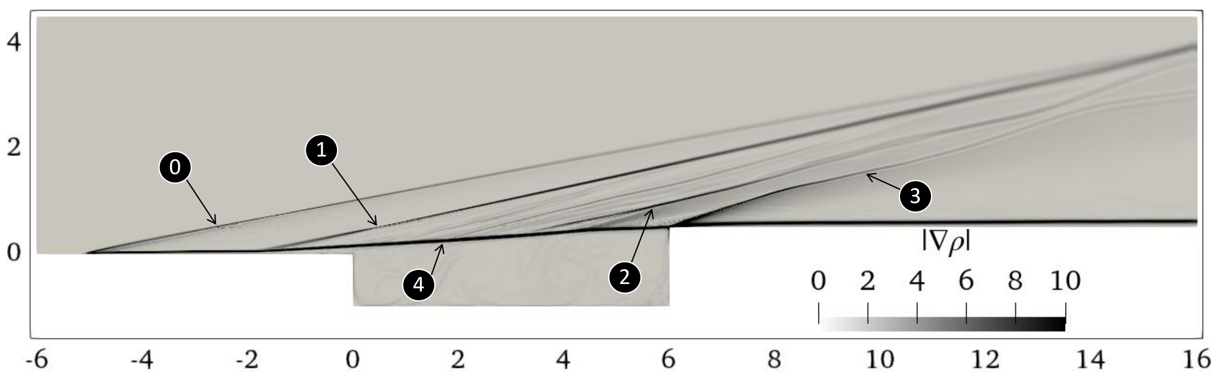

(c) Case 1.5h

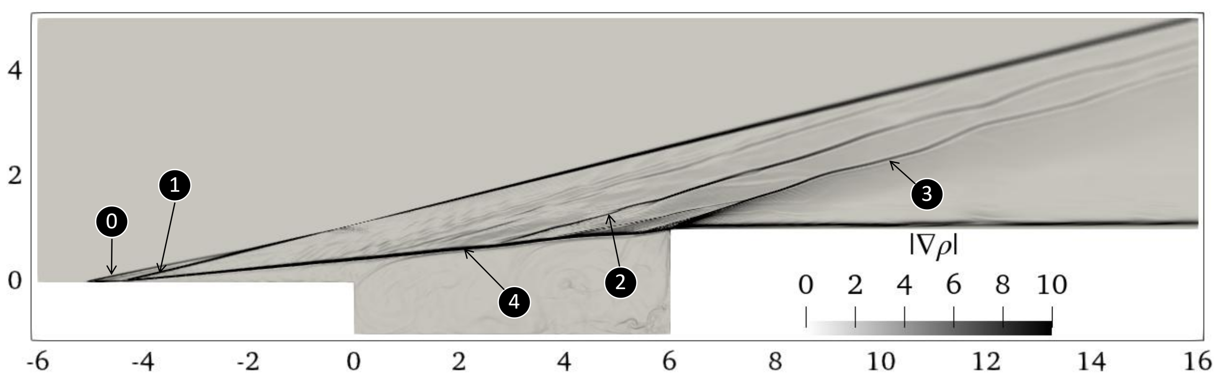

(d) Case 2.0h

Figure 6: Instantaneous numerical schlieren showing the identified flow features – (0) upstream-weak-shock wave, (1) leading-edge shock/expansion wave, (2) shock wave due to undulating shear layer, (3) trailing-edge impingement shock, (4) shear layer, and (5) lip shock.

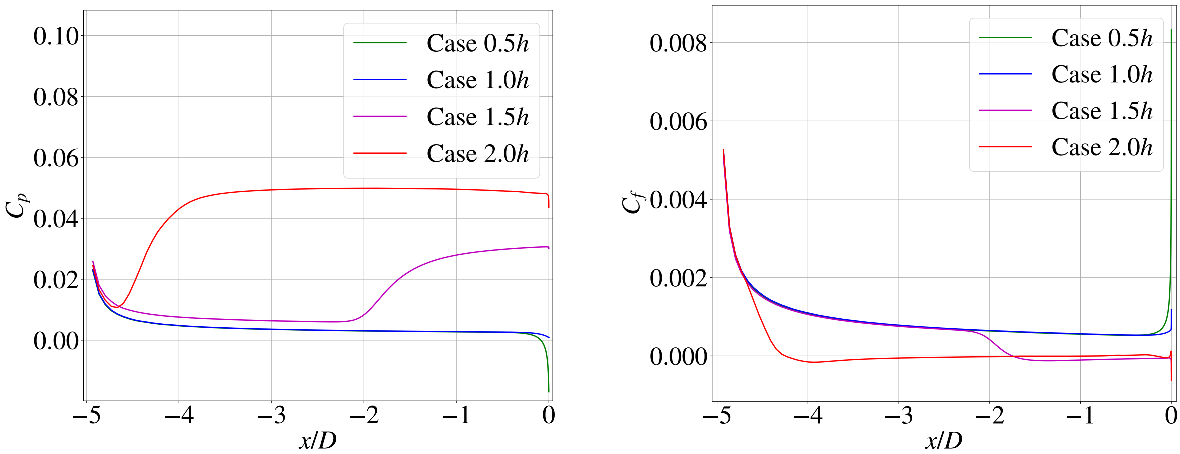

(a) C_p distribution on upstream wall (b) C_f distribution on upstream wall

Figure 7: Variation of (a) mean pressure coefficient, and (b) mean skin-friction coefficient C_f along the upstream wall for all the configurations studied.

with two distinct dominant oscillatory behaviors. Case $1.5h$ exhibits an initial high-amplitude Rossiter phase (Phase H) followed by an attenuated Rossiter phase (Phase A) where the fluctuation strengths are considerably reduced, whereas Case $2.0h$ experiences an initial Rossiter-dominated phase (Phase R) followed by the onset of low-frequency oscillation (Phase L). We refer to Phase H and Phase R as pre-transition phases and Phase A and Phase L as post-transition phases. The baseline configuration $1.0h$ shows no such behaviour. For both cases, this transition occurred only once during the time simulated. Thus, it is unclear if the pre-transition phase is a transient period before the flow eventually settles into a sustained long-time flow state or whether intermittent switching occurs due to spontaneous transition (e.g., due to bistability) if the simulations are continued for a longer simulation time. This has not been further investigated due to the computational cost. In the following discussion, first, the pre-transition phases are compared across configurations, following which the post-transition states are discussed in detail.

3.2.1 Pre-transition phase

The pre-transition phase for positive offset cases lasts for approximately ten flow-through times, indicating the long duration of this phase. Figure 9(a) presents the PSD of the vertical velocity fluctuations measured at approximately the center of the shear layer on the cavity centerline in the first pre-transition phase. Cases where there is no transition are also included for comparison. Note that the center's wall-normal coordinate changes with case, as the shear layer inclination varies with rear-wall height. The dominant frequencies are compared for increasing rear-wall height, h_r. Cases $1.0h$, $1.5h$ and $2.0h$ show a dominant peak at $St_h \approx 0.182$, 0.142, and 0.108, respectively, which approximately match the analytical estimates of the frequencies of the fifth (V), fourth (IV), and third (III) Rossiter modes. The analytical predictions are highlighted by the dashed lines, and are computed based on the modified Rossiter model proposed in Heller & Bliss [1]. Figure 9(b) presents the spectra of the dominant eigenvalues obtained from SPOD of the pressure fluctuation field for all configurations. The dominant energetic peaks are observed at Strouhal numbers $St_h \approx 0.183$, 0.142, and 0.108 for Cases $1.0h$, $1.5h$, and $2.0h$, respectively, similar to that observed in the PSD analysis. No dominant peaks are observed for Case $0.5h$ in the SPOD as well.

As the rear-wall height increases, the modes associated with lower Strouhal numbers (i.e., lower Rossiter modes) become dominant. Moreover, the configurations with higher rear-wall height contain more energy distributed across frequencies, as shown by the SPOD spectra, indicating that increasing the rear-wall height enhances the general flow unsteadiness across all frequencies, while also strengthening the low-

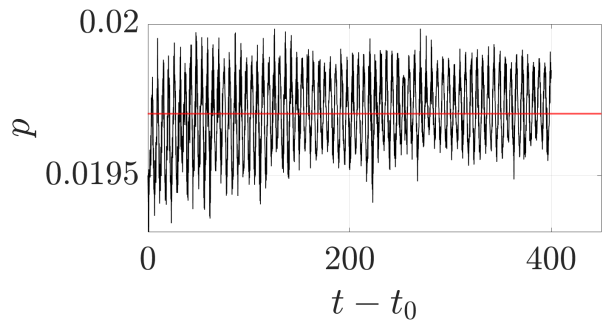

(a) Case $1.0h$

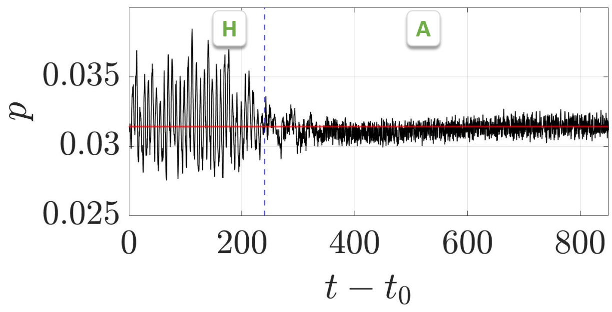

(b) Case $1.5h$

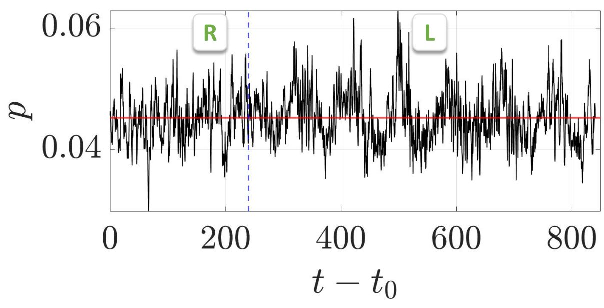

(c) Case $2.0h$

Figure 8: Pressure probe signals at (a) $(x/D = 3.0,\ y/D = -0.15)$, (b) $(x/D = 3.0,\ y/D = 0.1)$, and (c) $(x/D = 3.0,\ y/D = 0.5)$, corresponding to locations just beneath the shear layer for Cases $1.0h$, $1.5h$, and $2.0h$, respectively. The red horizontal line represents the temporal mean of the full signal, while the blue dashed line indicates the approximate location of the observed transition.

frequency Rossiter modes. Similarly, reducing the rear-wall height leads to a reduction in unsteadiness and a suppression of oscillations

The spatial structures of the SPOD modes (pressure fluctuations) for the dominant frequencies identified in the SPOD spectra are plotted in Figure 10 at an arbitrary time instant. The alternating convective structures and standing waves seen for all cases are typical of Rossiter modes. Case $1.0h$ exhibits five dominant spatial structures in the cavity region, corresponding to the fifth Rossiter mode, while Cases $1.5h$ and $2.0h$ show four and three dominant structures, corresponding to the fourth and third Rossiter modes, respectively. The spatial organization of these modes represents the self-sustained oscillation mechanism signature of cavity flows. Since Case $0.5h$ does not exhibit any distinct peak in the spectrum, no mode shape is presented for the same.

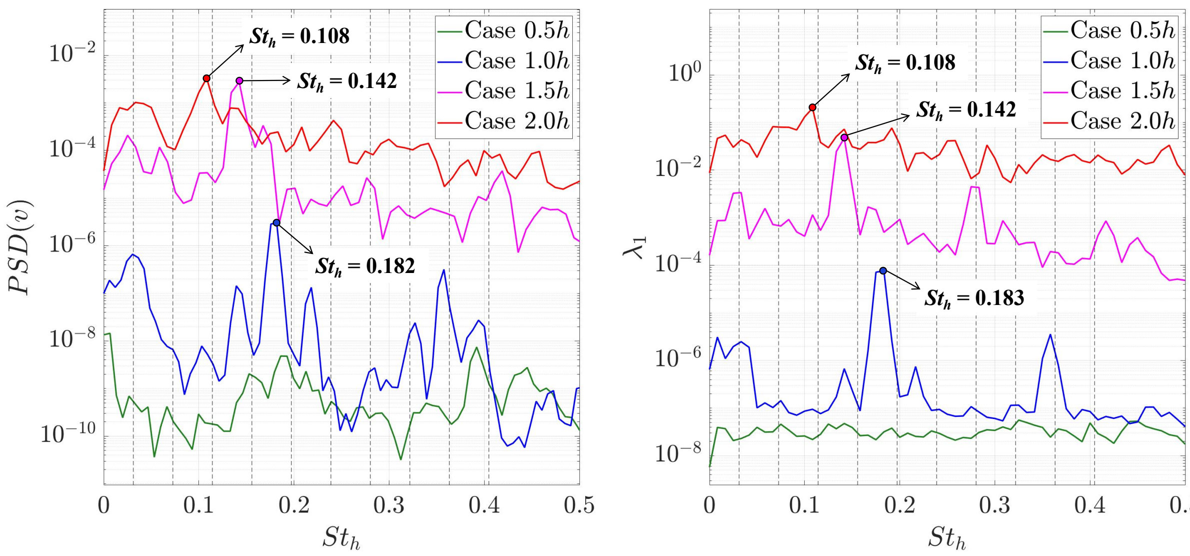

Figure 9: (a) Power spectral density of vertical velocity fluctuation in the shear layer for Cases $0.5h$ at $(3, -0.25)$, $1.0h$ at $(3, 0.05)$, $1.5h$ at $(3, 0.3)$ and $2.0h$ at $(3, 0.75)$. (b) Spectra of the dominant eigenvalue obtained from SPOD. The Strouhal numbers associated with Rossiter modes are highlighted using vertical dashed lines.

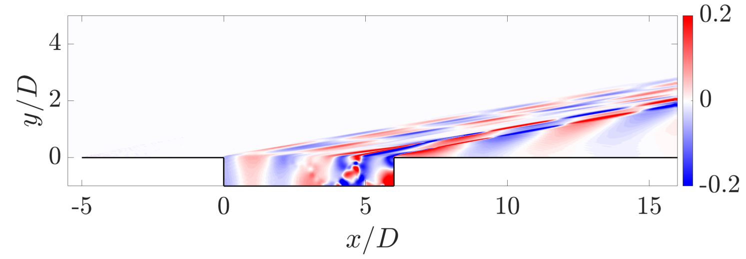

(a) Case $1.0h$ ($St_h \approx 0.183$)

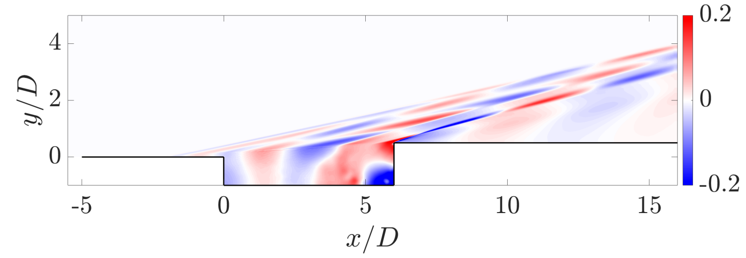

(b) Case $1.5h$ ($St_h \approx 0.138$)

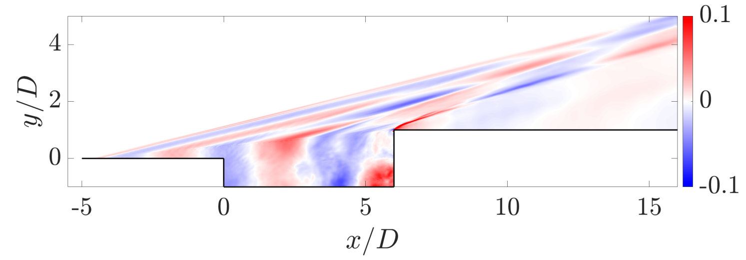

(c) Case $2.0h$ ($St_h \approx 0.108$)

Figure 10: Coherent structures obtained from the SPOD pressure field corresponding to the dominant peaks in the eigenvalue spectrum (Figure 9(b)) for (a) Case $1.0h$, (b) Case $1.5h$, and (c) Case $2.0h$.

3.2.2 Post-transition phase for Case 2.0*h*

For Case $1.5h$, post-transition, only the amplitude of oscillations of the dominant Rossiter mode reduces, while its frequency remains the same. By contrast, for Case $2.0h$, a new low-frequency phenomenon starts to dominate in the post-transition phase, which is examined in detail here. The eigenspectrum from SPOD of the pressure fluctuations for this case in the post-transition phase (Phase L) is compared with that of the pre-transition case (Phase R) in Figure 11. The SPOD spectra show a distinct peak at $St_h \approx 0.108$, for the Rossiter-dominated phase (Phase R), corresponding to Rossiter mode III. In contrast, the low-frequency dominated phase (Phase L) exhibits a strong dominant peak at $St_h \approx 0.012$ for Phase L. This peak occurs at a frequency that is lower than that of the lowest possible Rossiter mode I, indicating the emergence of a new oscillatory mode, which we will refer to as an LFO mode. Note that an additional secondary peak is noticed in this phase at $St_h \approx 0.061$, albeit of a lower energy than the LFO mode.

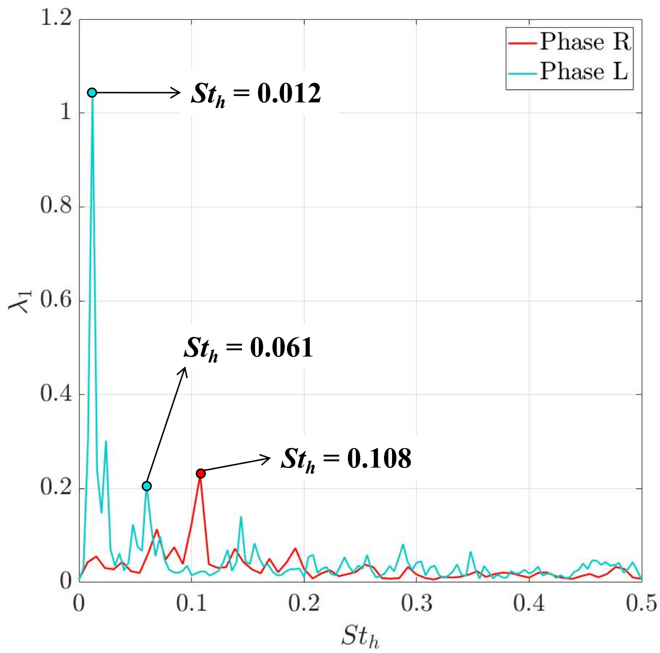

Figure 11: SPOD spectra of the dominant eigenvalues for R – Rossiter dominated phase (red) and L – low-frequency dominant phase (cyan), for Case $2.0h$

Figure 12 shows the corresponding spatial structures associated with the dominant peaks observed in the SPOD spectra at an arbitrary time. During the Rossiter-dominated phase, the spatial organization in Figure 12(a) reveals alternating convective patterns aligned along the length in the shear layer and within the cavity region, along with rear-wall impingement, representing the classical self-sustained Rossiter mechanism. By contrast, the low-frequency-dominated phase shows a large-scale organized structure occupying the entire cavity in Figure 12(b), with the upstream shock wave and separation region being out of phase with the flow within the cavity. This indicates that the shock wave and the separation point of the boundary layer are oscillating. Further, this LFO mode has relatively high energy content over a larger part of the domain, suggesting a more global influence than the Rossiter modes. The topological features of this LFO mode visually resemble the SPOD modes of transonic buffet, which is also characterized by large-scale oscillations of the shock wave and separation point at a low frequency [40]. The mode shape shown in Figure 12(c), corresponding to the secondary peak in Phase L, shows behaviour closer to Rossiter Mode II, although the energy contained in this mode is weak.

Figure 13 shows the spatio-temporal evolution of the skin-friction coefficient on the wall upstream of the cavity. The black contour denotes the locations at which $C_f = 0$, which is used to track the separation point. The plot shows that the LFO mode becomes fully developed at approximately $t - t_0 \approx 400$, following its onset at around $t - t_0 \approx 300$, causing the separation point to undergo large-amplitude

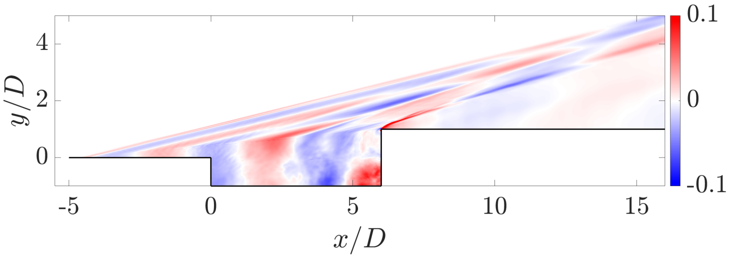

(a) Phase R ($St_h \approx 0.108$)

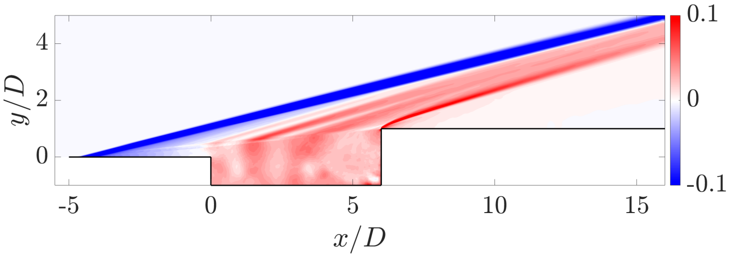

(b) Phase L ($St_h \approx 0.012$)

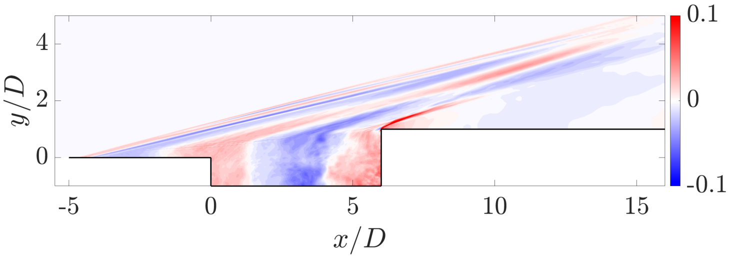

(c) Phase L ($St_h \approx 0.061$)

Figure 12: Coherent structures obtained from the SPOD pressure field corresponding to the dominant peaks in the eigenvalue spectrum (Figure 11) for Case $2.0h$: (a) Rossiter mode, (b) LFO mode, and (c) secondary peak during LFO-dominated state.

periodic streamwise oscillations. During this period, the separation point oscillates between $x = -4.7h$ and $x = -3.85h$. Once established, the low-frequency oscillation persists throughout the remainder of the simulation duration, confirming that the low-frequency oscillation is the dominant mechanism governing the cavity flow dynamics.

4. Conclusion and Future Work

The effect of rear-wall height variation on hypersonic open-cavity flows has been investigated through high-fidelity simulations using a GPU-accelerated flow solver, OpenSBLI. The two-dimensional numerical simulations show that increasing the rear-wall's height results in the upstream migration of the mean separation location, with the mean separation extent relative to the leading edge of the cavity being directly proportional to the rear-wall height. The rear-wall height also affects the oscillatory characteristics of the flow, with the dominant Rossiter modes shifting to lower mode numbers with increasing rear-wall height. While Case $0.5h$ does not exhibit a distinct oscillatory behaviour, configurations with rear-wall heights of $1.0h$, and $1.5h$ remain governed by the classical Rossiter feedback mechanism, whereas for $2.0h$, a transition to low-frequency oscillations (LFO) is observed. The features of this LFO state were extracted using a spectral proper orthogonal decomposition (SPOD). The spatial features of the SPOD mode corresponding to LFO exhibit an out-of-phase relation between the pressure in the vicinity of the shock wave and that in the entire cavity. Additionally, this LFO mode was characterized by distinct large-scale periodic variation in which the point of separation of the boundary layer on the upstream plate

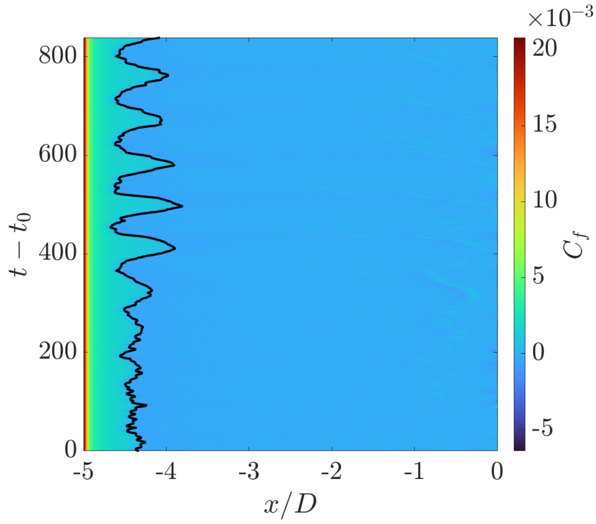

Figure 13: Space-time diagram of the skin-friction coefficient on the upstream wall for Case $2.0h$. The black contour denotes the instantaneous separation location ($C_f = 0$).

oscillates. Thus, it is shown that the rear-wall height can not only affect the Rossiter mode selected but can also modify the fundamental oscillation mechanism in a cavity flow. Efforts to extend the present two-dimensional simulations to three dimensions to gain further insight into the turbulent characteristics of the flow and LFO are ongoing. Future work will involve investigating the physical mechanism responsible for the onset of the low-frequency oscillation and identifying the critical geometric conditions that cause the transition. The insights gained from the present study can potentially aid in the better design of hypersonic vehicles and also be harnessed for hypersonic combustion.

Acknowledgements

The authors acknowledge the computational resources provided by the PARAM Sanganak supercomputing facility at the Indian Institute of Technology Kanpur, India, which was used to perform the simulations presented in this work. The computational and experimental resources required for the study were facilitated through the Start-up Research Grant (Project number: SRG/2023/000438), and Ramanujan Fellowship Grant (Project number: RJF/2023/000042) awarded by the Science and Engineering Research Board (currently, Anusandhan National Research Foundation), India.

References

[1] H. Heller and D. Bliss. The physical mechanism of flow-induced pressure fluctuations in cavities and concepts for their suppression. AIAA Paper, 2nd Aeroacoustics Conference, 1975.

[2] J. E. Rossiter. Wind-tunnel experiments on the flow over rectangular cavities at subsonic and transonic speeds. Reports and Memoranda 3438, Aeronautical Research Council, London, United Kingdom, 1964.

[3] A. Malhotra and A. Vaidyanathan. Aft wall offset effects on open cavities in confined supersonic flow. *Experimental Thermal and Fluid Science*, 74:411–428, 2016.

[4] K. Karamcheti. Acoustic radiation from two-dimensional rectangular cutouts in aerodynamic surfaces. NACA Technical Note NACA TN-3487, National Advisory Committee for Aeronautics (NACA), Washington, D.C., USA, 1955.

[5] E. B. Plentovich, Robert L. Stallings Jr., and M. B. Tracy. Experimental cavity pressure measurements at subsonic and transonic speeds: Static-pressure results. NASA Technical Paper NASA TP-3358, NASA Langley Research Center, 1993.

[6] Robert L. Stallings Jr. and Floyd J. Wilcox Jr. Experimental cavity pressure distributions at supersonic speeds. NASA Technical Paper NASA TP-2683, NASA Langley Research Center, 1987.

[7] D. S. Dolling, S.-W. Perng, and Y. L. Leu. An experimental study of passive control of hypersonic cavity flow oscillations. Technical Report AFRL-SR-BL-TR-98-0240, Center for Aeromechanics Research, University of Texas at Austin, 1997.

[8] S.J. Lawson and G.N. Barakos. Review of numerical simulations for high-speed, turbulent cavity flows. *Progress in Aerospace Sciences*, 47(3):186–216, 2011.

[9] C. O. L. H. Smith, N. Lawson, and G. A. Vio. History, review and summary of the cavity flow phenomena. *European Journal of Mechanics - B/Fluids*, 108:32–72, 2024.

[10] N. Zhuang, F. S. Alvi, M. B. Alkislar, and C. Shih. Supersonic cavity flows and their control. *AIAA Journal*, 44(9):2118–2128, 2006.

[11] C. W. Rowley, T. Colonius, and A. J. Basu. On self-sustained oscillations in two-dimensional compressible flow over rectangular cavities. *Journal of Fluid Mechanics*, 455:315–346, 2002.

[12] S. Singh and L. Ukeiley. Proper orthogonal decomposition of high-speed particle image velocimetry in an open cavity. *AIAA Journal*, 58:1–16, 03 2020.

[13] P. S. Doshi, R. Ranjan, and D. V. Gaitonde. Global and local modal characteristics of supersonic open cavity flows. *Physics of Fluids*, 34(3):034104, April 2022.

[14] H. Wang, M. Sun, N. Qin, H. Wu, and Z. Wang. Characteristics of oscillations in supersonic open cavity flows. *Flow, Turbulence and Combustion*, 90(1):121–142, 2013.

[15] R. C. Murray and G. S. Elliott. Characteristics of the compressible shear layer over a cavity. *AIAA Journal*, 39(5):846–856, 2001.

[16] A. Morgenstern and N. Chokani. Hypersonic flow past open cavities. *AIAA Journal*, 32(12):2387–2393, 1994.

[17] O. H. Unalmis, N. T. Clemens, and D. S. Dolling. Experimental study of shear-layer/acoustics coupling in mach 5 cavity flow. *AIAA Journal*, 39(2):242–252, 2001.

[18] T. Bai, Z. Duan, and Z. Xiao. Depth effects on the cavity induced transition at hypersonic speed by dns. *International Journal of Heat and Fluid Flow*, 97:109028, 2022.

[19] E. B. Plentovich, J. Chu, and M. B. Tracy. Effects of yaw angle and reynolds number on rectangular-box cavities at subsonic and transonic speeds. NASA Technical Paper NASA TP-3099, NASA Langley Research Center, 1991.

[20] M. B. Tracy, E. B. Plentovich, and J. Chu. Measurements of fluctuating pressure in a rectangular cavity in transonic flow at high reynolds numbers. NASA Technical Memorandum NASA TM-4363, NASA Langley Research Center, 1992.

[21] J. Scheiman. Acoustic measurements of a large cavity in a wind tunnel. NASA Technical Memorandum NASA TM-78658, NASA Langley Research Center, Hampton, Virginia, USA, 1978.

[22] A. Seena and H. J. Sung. Dynamic mode decomposition of turbulent cavity flows for self-sustained oscillations. *International Journal of Heat and Fluid Flow*, 32(6):1098–1110, 2011.

[23] Y. Sun, Q. Liu, L. N. Cattafesta, L. S. Ukeiley, and K. Taira. Effects of sidewalls and leading-edge blowing on flows over long rectangular cavities. *AIAA Journal*, 57(1):106–119, 2019.

[24] J. Malone, M. Debiasi, J. Little, and M. Samimy. Analysis of the spectral relationships of cavity tones in subsonic resonant cavity flows. *Physics of Fluids*, 21(5):055103, May 2009.

[25] S. Lawson, George Barakos, and A. Simpson. Understanding cavity flows using proper orthogonal decomposition and signal processing. *Journal of Algorithms & Computational Technology*, 4:47–70, 03 2010.

[26] Z. Ren, B. Wang, B. Hu, and L. Zheng. Numerical analysis of supersonic flows over an aft-ramped open-mode cavity. *Aerospace Science and Technology*, 78:427–437, 2018.

[27] N. S. Vikramaditya and J. Kurian. Effect of aft wall slope on cavity pressure oscillations in supersonic flows. *The Aeronautical Journal*, 113(1143):291–300, 2009.

[28] V. M. Don. *Computational Investigation of Supersonic Cavity Flows and Passive Controls*. PhD thesis, School of Engineering and Materials Science, Queen Mary University of London, London, 2021.

[29] R. E. Dix and C. Butler. Cavity aeroacoustics. Technical Report AFATL-TP-90-08, Air Force Armament Laboratory, 1990.

[30] R. E. Dix and R. C. Bauer. Experimental and theoretical study of cavity acoustics. Technical Report AEDC-TR-99-4, Arnold Engineering Development Center, 2000.

[31] S. R. Nanda, T. V. Krishna, S. K. Karthick, and J. Cohen. Axisymmetric cavities in hypersonic flow, 2026.

[32] D. J. Lusher, A. Sansica, N. D. Sandham, J. Meng, B. Siklósi, and A. Hashimoto. Opensbli v3.0: High-fidelity multi-block transonic aerofoil cfd simulations using domain specific languages on gpus. *Computer Physics Communications*, 307:109406, 2025.

[33] A. Hamzehloo, D. J. Lusher, and N. D. Sandham. Direct numerical simulations and spectral proper orthogonal decomposition analysis of shocklet-containing turbulent channel counter-flows. *International Journal of Heat and Fluid Flow*, 104, DEC 2023.

[34] A. Gillespie and N. D. Sandham. Numerical study of the effect of sidewalls on shock train behaviour. *Flow*, 3, MAY 12 2023.

[35] D.J. Lusher, S. P. Jammy, and N. D. Sandham. OpenSBLI: Automated code-generation for heterogeneous computing architectures applied to compressible fluid dynamics on structured grids. *Computer Physics Communications*, 267:108063, 2021.

[36] D. J. Lusher and N. D. Sandham. Shock-wave/boundary-layer interactions in transitional rectangular duct flows. *Flow Turbulence and Combustion*, 105(2, SI):649–670, AUG 2020.

[37] A. Hamzehloo, D. J. Lusher, S. Laizet, and N. D. Sandham. On the performance of weno/teno schemes to resolve turbulence in dns/les of high-speed compressible flows. *International Journal for Numerical Methods in Fluids*, 93(1):176–196, JAN 2021.

[38] D. J. Lusher, S. P. Jammy, and N. D. Sandham. Shock-wave/boundary-layer interactions in the automatic source-code generation framework OpenSBLI. *Computers & Fluids*, 173:17–21, SEP 15 2018.

[39] C. Zhang, R. Li, Z. Xi, Z. Wan, and D. Sun. Effect of mach number on the mode transition for supersonic cavity flows. *Aerospace Science and Technology*, 106:106101, 2020.

[40] P. Moise, M. Zauner, and N. D. Sandham. Connecting transonic buffet with incompressible low-frequency oscillations on aerofoils. *Journal of Fluid Mechanics*, 981:A23, 2024.